Nanoscale

PAPER

View Article Online
View Journal | View Issue

Cite this: *Nanoscale*, 2025, **17**, 20280

Impact of Bi^{3+} and Cu^{2+} doping on the optical and electronic properties of $CsPbBr_3$ for photocatalytic toluene oxidation

Marija Knezevic,†[a] Thi-Hieu Hoang,†[a] Vien Duong Quach, [a] Alba Garzón Manjón,[c] David Llorens Rauret, [c] Marie Erard,[a] Audrey Gayral,[a] Mireille Benoit,[a] David Berardan, [b] Jordi Arbiol, [c,d] Christophe Colbeau-Justin[a] and Mohamed Nawfal Ghazzal *[a]

Received 8th June 2025,
Accepted 25th July 2025

DOI: 10.1039/d5nr02442k

rsc.li/nanoscale

Doping of metal halide perovskites (MHPs) offers an opportunity to introduce trap states that are reported to be beneficial for the charge carrier dynamics. Herein, we investigated the electronic structure–photocatalytic relationship of $CsPbBr_3$ doped with Bi^{3+} and Cu^{2+} cations. Bi doping necessitates a reduction in the hot-injection temperature to avoid the formation of Bi nanoparticles, leading to the formation of two-dimensional $CsPbBr_3$ with a variable aspect ratio. Bi doping causes no significant changes in the band gap energy but leads to the gradual appearance of a band-tail in the absorbance spectrum and a broad-band emission peak covering a large wavelength range. A photoluminescent quenching is observed as the ratio of Bi^{3+} increases, indicating shallow trap generation. Cu^{2+} doping does not affect the morphology of the 3D crystalline $CsPbBr_3$ and shows a photoluminescent blueshift, which translates to a change in the bandgap energy. The $CsPbBr_3$ doping, with an adequate amount of Cu, provides the best photocatalytic activity, surpassing Bi-doped $CsPbBr_3$. Time-resolved photoluminescence analysis indicated that Bi^{3+} introduces a shallow trap that captures electrons while leaving the holes free, leading to an increase in the charge carrier lifetime, thus favoring charge carrier separation. Unlike bismuth, Cu^{2+} affects both the conduction and valence band positions, making the oxidation reaction more favorable.

Introduction

Metal halide perovskites (MHPs) have renewed the interest in solar energy conversion since they were included in dye-sensitized solar cells and other solar cell technologies.[1,2] MHPs have versatile properties that offer plenty of possibilities to control their optoelectronic properties and light-harvesting capabilities.[3] The most commonly reported is the partial anion substitution (Br_{1-x}/Cl_x or Br_{1-x}/I_x), which is an excellent way to tune the optical and electronic bandgaps of perovskites, leading to the fine control of photoluminescence, charge-carrier transfer, and photocatalytic properties.[4] Partial halide substitution leads to an upward shift in the valence band maximum (VBM) and a downward shift in the conduction band minimum (CBM) as both have a contribution from the halide antibonding orbitals.[5,6] Cation substitution has been envisaged mainly to diminish the toxicity of MHPs due to the presence of Pb in their structure.[7] Partial replacement of Pb^{2+} cations in $CsPbBr_3$ QDs with Sn^{2+}, Cd^{2+}, and Zn^{2+} was achieved by post-synthetic cation exchange.[8,9] A partial substitution of Pb leads to either PL enhancement or quenching, depending on the oxidation potential of the metallic cation and whether or not the trap states are introduced.[7,10,11] In addition, the complete replacement of lead through single and bimetallic substitution (Ag, Bi, Sn, and Sb) resulted in the formation of 2D double perovskites (A_2MX_6, $A_3M_2X_6$, and $A_2M^1M^2X_6$).[12–14] On the contrary, divalent and trivalent cations, such as Mn, Ni, Cu, Al, Ce, and Bi, could affect structural, optical, and electronic properties while retaining either the cubic or orthorhombic crystal structure of MHPs.[10,11,15–17] The trivalent Bi^{3+} and Pb^{2+} have very close ionic radii and are isoelectronic ($6s^2$). Bi^{3+} was employed to substitute Pb^{2+} and reduce the toxicity of 2D perovskite structures, which have shown enhanced photoactivity, *e.g.*, 0D bismuth-based halide double perovskites such

---

[a] *Université Paris-Saclay, UMR 8000 CNRS, Institut de Chimie Physique, 91405 Orsay, France. E-mail: mohamed-nawfal.ghazzal@universite-paris-saclay.fr*
[b] *Université Paris-Saclay, UMR 8182 CNRS, Institut de chimie moleculaire, F-91405 Orsay, France*
[c] *Catalan Institute of Nanoscience and Nanotechnology (ICN2), CSIC and BIST, Campus UAB, Bellaterra, 08193 Barcelona, Catalonia, Spain*
[d] *ICREA, Pg. Lluís Companys 23, 08010 Barcelona, Catalonia, Spain*

† These authors contributed equally.

as $Cs_3Bi_2I_9$,[18] $Cs_3Bi_2X_9$ embedded in mesoporous silica ($Cs_3Bi_2X_9$-SBA-15),[19] and $Cs_3Bi_2X_9$ coupled with graphitic carbon nitride ($Cs_3Bi_2X_9$-g-C_3N_4).[20] Moreover, 2D $Cs_3Bi_2X_9$ and $Cs_3Bi_2X_9$-g-C_3N_4-Pt demonstrated interesting activity for H_2 production from pure ethanol and 10% v/v aqueous triethanolamine, respectively.[21,22] From another point of view, Bi-doped hybrid or inorganic perovskites have demonstrated promising optical and electronic properties.[23–25] For example, doping $CsPbBr_3$ perovskite nanocrystals with Bi^{3+} ions led to photoluminescence quantum yield (PLQY) quenching and a potential change in the bandgap energy.[16] However, this change in bandgap energy has been questioned. In particular, the combination of spectroscopic ellipsometry and transmission spectroscopy suggested that the change in the absorption onset does not rationalize the change in the optical bandgap. Further direct measurement of the bandgap of Bi-doped $CsPbBr_3$ using angle-resolved photoelectron spectroscopy revealed no change in the valence band energy.[26] Upon Bi doping, the photoluminescence (PL) quenching was instead confirmed and associated with the formation of trap states that enhance electron trapping and suppress radiative recombination.[26] In the same context, copper, with a smaller ionic radius (73 pm) compared to Pb^{2+} (119 pm), is another potential dopant for MHPs. Doping mixed-halide perovskites with divalent Cu^{2+} ions was reported to increase lattice binding energy and improve the short-range order of the lattice, which was identified as a factor improving both the thermal stability and PLQYs.[7] The crystal lattice contraction through partial substitution of Pb^{2+} with Cu^{2+} and a reduction in surface energy in two-dimensional $CsPbBr_3$ perovskite nanoplatelets after Cu doping lead to long-term stability and photostability under ambient conditions. Although Cu-doped all-inorganic perovskites have primarily been studied for their photoluminescence properties, there is limited research on their photocatalytic properties. To the best of our knowledge, only the photocatalytic activity of Cu/$CsPbBr_3$–Cs_4PbBr_6 nanocrystals (NCs) has been studied.[27]

Herein, we investigated the effect of $CsPbBr_3$ doping with bi- and tri-valent cations on its electronic and photocatalytic properties. This choice was motivated by the fact that Bi and Cu doping affect charge carriers differently, which is a determining parameter expected to modify the photocatalytic activity. Indeed, Bi has been reported to quench the PL, whereas Cu doping is more likely to enhance it. Thus, chemical, morphological, structural, optical, and electronic properties were investigated after the doping. Interestingly, varying the valence state of the dopants led to different effects, imparting each perovskite with specific properties. For instance, a drastic change in the morphology and the optical response was observed with Bi doping, whereas the perovskite maintained its morphology once doped with Cu. The charge carrier lifetime was determined using time-resolved laser scanning time-correlated single photon counting (TCSPC) microscopy, suggesting that both Cu and Bi doping could introduce shallow defects, thus affecting the photocatalytic efficiency in toluene oxidation.

Experimental section

Materials

All chemicals were used as received, without further purification or modification. Cesium carbonate (Cs_2CO_3, 99.5%), lead bromide ($PbBr_2$, 99%), and oleylamine (OAm, 80%–90%) were purchased from Acros Organics. Oleic acid (OA) was obtained from Riedel de Haën. Toluene (99.8%), tetrabutylammonium hexafluorophosphate ((Bu_4N)(PF_6), ≥98%), dichloromethane (DCM, ≥99.8%), 1-octadecene (ODE, 90%), *n*-hexane (95%), and acetonitrile (CH_3CN, ≥99.9%, for HPLC) were purchased from Sigma-Aldrich.

Synthesis of phase-pure $CsPbBr_3$

$CsPbBr_3$ nanocrystals were synthesized following a previously reported procedure.[28,29] Briefly, Cs-oleate was prepared by mixing pre-dried Cs_2CO_3 (0.163 g), OA (1.58 mL), and ODE (3.42 mL) at 120 °C under an argon flow for 1 h with vigorous stirring at 500 rpm. In order to completely dissolve Cs_2CO_3, the temperature was increased up to 130 °C at a rate of 1 °C min^{-1}. Cs-oleate must be preheated to 120 °C before use in the synthesis of $CsPbBr_3$ to avoid precipitation at room temperature. Simultaneously, $PbBr_2$ (0.21 g), OA (1.5 mL), OAm (1.5 mL), and ODE (5 mL) were mixed and heated at 120 °C under an argon flow for 1 h. After complete dissolution of $PbBr_2$, the temperature was raised to 200 °C. The previously prepared and preheated solution of Cs-oleate was then injected (0.75 mL). The reaction was immediately quenched by immersing the flask in an ice/water bath. $CsPbBr_3$ was dispersed in toluene and centrifuged at 7500 rpm for 20 min. The supernatant was discarded, and $CsPbBr_3$ NCs were washed three times with *n*-hexane (total 10 mL) and centrifuged again at 7500 rpm for 10 min. After the removal of aggregates, the elaborated $CsPbBr_3$ was dispersed in *n*-hexane.

Synthesis of Bi-doped $CsPbBr_3$ nanocrystals

The bismuth-doped $CsPbBr_3$ MHPs were synthesized by adapting the synthetic procedure used for pristine $CsPbBr_3$. Bi doping was introduced by partially substituting Pb^{2+} with Bi^{3+} to yield $Cs_2Pb_{1-x}Bi_xBr_3$ compositions, where x = 0.01, 0.02, 0.05, and 0.10, corresponding to 1, 2, 5, and 10 mol% of Bi relative to the total B-site cations (Pb + Bi). The amount of $PbBr_2$ was fixed at 0.21 g, and the mass of $BiBr_3$ was varied accordingly to achieve the desired stoichiometric ratios. The variable mass ratio of $BiBr_3$ and $PbBr_2$ was mixed with OA (3 mL), OAm (1.5 mL), and ODE (10 mL), and heated at 120 °C, stirring at 500 rpm under argon flow for 1 h. After the complete dissolution of $BiBr_3$ and $PbBr_2$, the temperature was increased to 160 °C at a rate of 1 °C min^{-1}. The previously prepared and preheated solution of Cs-oleate was injected (0.75 mL). The reaction was immediately quenched by immersing the flask in an ice/water bath. The purification process using hexane and toluene for the bismuth-doped $CsPbBr_3$ was identical to that of the pristine $CsPbBr_3$. The synthesis of bismuth-doped $CsPbBr_3$ was also carried out at 200 °C, using equivalent amounts of OA (3 mL), OAm (3 mL), and ODE (10 mL).

Synthesis of Cu-doped $CsPbBr_3$ nanocrystals

The copper-doped $CsPbBr_3$ was synthesized by mixing a variable molar ratio (Pb : Cu = 1 : 0.25, 1 : 0.5, 1 : 1, 1 : 1.5) of $CuBr_2$ and $PbBr_2$ (0.21 g) with OA (1.5 mL), OAm (1.5 mL), and ODE (10 mL), and heating the mixture at 120 °C under argon flow for 1 h. After the dissolution of $CuBr_2$ and $PbBr_2$, the temperature was increased to 200 °C. The previously prepared and preheated solution of Cs-oleate (0.75 mL) was injected. The reaction was immediately quenched by immersing the flask in an ice/water bath. The purification process with hexane and toluene was identical to that of pristine $CsPbBr_3$.

Characterization techniques

Diffuse reflectance spectra (DRS) were recorded using a UV-vis-NIR Cary 5000 spectrophotometer (Agilent Technologies) equipped with an integrating sphere for diffuse and total reflection measurements. The maximum reflectance was set to 100% using $BaSO_4$ as a reference in the 200 to 1100 nm wavelength range.

Photoluminescence (PL) emission spectra were recorded using a Fluorolog-3 spectrofluorometer (HORIBA) equipped with a solid-state sample holder. All samples were excited at 400 nm, and emission spectra were monitored over the 450 to 700 nm range.

X-ray photoelectron spectroscopy (XPS). Measurements were performed on a K-Alpha spectrometer from ThermoFisher, equipped with a monochromated X-ray Source (Al Kα, 1486.6 eV) with a spot size of 400 μm. The hemispherical analyzer was operated in constant analyser energy (CAE) mode, with a pass energy of 200 eV and a step size of 1 eV for the acquisition of survey spectra, whereas for the acquisition of narrow scans, a pass energy of 50 eV and 100 eV and a step size of 0.1 eV were used. The 50 eV pass energy was utilized for core levels requiring high spectral resolution to accurately resolve chemical shifts and fine structure, as seen with Bi 4f and Cu 2p. In contrast, we applied a pass energy of 100 eV for core levels characterized by lower signal intensity or overlapping peaks. This approach allowed us to enhance signal strength while still maintaining a reasonable level of resolution.

The charge build-up was neutralized by a "dual-beam" flood gun. The obtained spectra were treated using CasaXPS software. The binding energies were calibrated against the C 1s binding energy set at 284.8 eV.

Powder X-ray diffraction (PXRD) patterns were recorded using a room-temperature powder X-ray diffractometer. Patterns were recorded by a Panalytical X'Pert diffractometer equipped with a Ge(111) incident monochromator (Cu-Kα radiation) and an X'celerator detector.

Transmission electron microscopy (TEM). The TEM and HRTEM images were obtained using a JEOL JEM 2100Plus operating at 200 kV and a Tecnai F20 field emission gun (FEG) microscope at 200 kV. The size of synthesized nanostructures was measured using Gatan Digital Micrograph software. All the crystal lattices in the micrographs of interest were enhanced using a frequency filter in the reciprocal space.

Electron energy loss spectroscopy (EELS). Compositional analysis was conducted using a double-corrected and monochromated Thermo Fisher Spectra 300 microscope operated at 300 kV. For elemental mapping and quantification studies, the L edges of Br and $M_{4,5}$ edges of Cs and Pb were used. To reduce noise in the EELS spectra, principal component analysis (PCA) was conducted, followed by reconstruction using a sufficient number of components to prevent data loss. EELS data analysis was conducted using Gatan Digital Micrograph software.

Time-resolved photoluminescence lifetime measurements were carried out with a homemade setup. All samples were excited at 370 nm (80 ps FWHM, 10 MHz, PicoQuant). The instrument response function was determined by the excitation of colloidal silica (SiO_2, Ludox) at 370 nm. The emitted luminescence was selected using a monochromator (ARC Spectra drive) at 517 ± 5 nm and detected by an MCP-PMT (Hamamatsu) connected to a PicoHarp 300 TCSPC module (PicoQuant). Lifetime measurements were analyzed using the SymPhoTime software (PicoQuant).

Cyclic voltammetry (CV) measurements were carried out using $(Bu_4N)(PF_6)$ 0.1 M in dichloromethane (DCM) as the electrolyte. The formal potential of the non-aqueous reference electrode $Ag|Ag^+$ was calibrated by adding 2 mM ferrocene/ferrocenium (Fc/Fc^+) as an internal standard at the end of the measurements. All measurements were carried out using a PGSTAT101 Metrohm Autolab potentiostat.

Photocatalytic oxidation of toluene was performed by dispersing 3 mg of Bi-doped and Cu-doped $CsPbBr_3$ NCs in 3 mL of toluene in a quartz reactor. The obtained dispersion was purged with a continuous flow of oxygen gas for 20 min. The samples were irradiated using an Oriel 300 W xenon lamp equipped with an infrared water filter for 3 h under stirring. The aliquots were taken every 30 min and analyzed using high-performance liquid chromatography (HPLC).

Results and discussion

We prepared undoped and doped $CsPbBr_3$ by a hot-injection method. The obtained Cu-$CsPbBr_3$ nanoparticles demonstrated a similar yellow color with varying $PbBr_2/CuBr_2$ ratios in the crude solution, *i.e.*, the molar ratio of Pb/Cu was set to 0.25, 0.5, 1.0, and 1.5. Cu doping of MHPs required a significant amount of Cu(II) precursor due to the higher formation energy of Cu–Br compared to Pb–Br, *e.g.*, −14.2 eV for $CsCuBr_3$, −6.82 eV for $CsPb_{0.93}Cu_{0.07}Br_3$, and −6.56 eV for $CsPbBr_3$.[7] Bismuth-doped cesium-lead bromide (hereafter Bi-$CsPbBr_3$) nanoparticles were first synthesized at 200 °C by a hot-injection method. Higher temperatures were found to induce the reduction of Bi precursors and the formation of bismuth nanoparticles alongside perovskite nanocrystals (Fig. S1). Bismuth reduction occurred at high temperatures in a cesium-free solution in the presence of reductive agents and capping agents essential for controlling the size of MHPs, such as OA and OAm.[30–32] Thus, the synthesis temperature was decreased to 160 °C, and the ratio of OA to OAm was adjusted (1 : 2) to avoid thermal reduction of bismuth.[33,34] The color of the obtained Bi-$CsPbBr_3$ nanoparticles changed from yellow ($CsPbBr_3$) to dark orange ($CsPb_{0.90}Bi_{0.10}Br_3$ – all compositions given in the article are nominal compositions), as the amount of Bi in the crude solution increased (1%, 2%, 5%, and 10%) (Fig. 1).

The absorbance spectra show that the excitonic band remains unaffected upon doping (Fig. 2a). Cu doping results in a blue-shifted emission as the molar ratio of Cu increases, compared with the pristine $CsPbBr_3$ (Fig. 2b), which is in agreement with previous reports.[7,35] The Kubelka–Munk calculation indicates no significant change in the optical bandgap (Fig. S2), which contrasts with the PL shift to a shorter wavelength (Fig. 2b). Cyclic voltammetry measurements were carried out for all samples, demonstrating changes in the potential energies of the VBM and CBM (Fig. 2c). The bandgap energy of $CsPbBr_3$ increases from 2.31 eV to 2.50 eV upon Cu doping (Fig. 2d), aligning with the PL results. We attributed this discrepancy to the additional states introduced as shallow trap states in the CBM, which could not be observed in UV-Vis spectroscopy.

Before discussing the Bi doping, we recorded the PL spectra of undoped $CsPbBr_3$ synthesized at different temperatures (160 °C and 200 °C) and at 160 °C with an excess OA to enhance the solubility of the bismuth precursor (Fig. 3a). A blue shift of 11 nm in the PL maximum was observed when the synthesis temperature was lowered. An additional shift of 6 nm was noted when excess OA was used. Interestingly, the PL spectrum of the MHP synthesized with excess OA exhibited three additional emission peaks with lower intensity. The lowest-energy emission peak at 460 nm could be attributed to biexciton (BX), while the highest-energy exciton at 491 nm could be assigned to the active bright band (DX).[36,37] This PL emission behavior is typically observed in 2D perovskites.[36,37] The PL spectra of Bi-doped $CsPbBr_3$ displayed a broad emission band covering a large emission range between 420 and 540 nm (Fig. 3b). The band edge emission was found to be composite, consisting of multi-emission peaks centered at 430, 465, 480, 490, and 520 nm, with the intensity decreasing as the Bi content increased. Additional emission peaks appear compared to undoped $CsPbBr_3$, suggesting a supplementary excitonic phenomenon that could not be assigned at this stage. As the doping ratio increases from 1% to 2%, the peaks at 490 and 520 nm are quenched. At a higher doping ratio (10%), all peaks disappeared, and a new band edge emission appeared at 435 nm. Upon Bi doping, the excitonic absorption band is observed around 540 nm, similar to that of undoped $CsPbBr_3$. Further increase in the Bi ratio leads to the gradual appearance of a band-tail in the absorbance spectrum, as shown in Fig. 3c. We evaluated the bandgap energy using the Kubelka–Munk function, and all Bi-$CsPbBr_3$ samples demonstrated bandgap energies in the range of 2.2–2.3 eV (Fig. S2b). The conduction and valence band positions were determined using cyclic voltammetry measurements (Fig. S3). The obtained values, shown in Fig. 3d, are slightly higher than values obtained using the Kubelka–Munk calculation, falling in the range of 2.40–2.46 eV. This discrepancy is due to the presence of multi-emission peaks and the formation of trap states, which may account for the band-tail observed in the 550–700 nm range of the absorbance spectrum.[38,39] Note that the optical bandgap describes the transition of the excitonic band of the electron–hole pair (eqn (1)):

$$E_{\mathrm{opt}} = E_{\mathrm{g}} + E_{\mathrm{b}} \tag{1}$$

where E_{b} represents the exciton binding energy and E_{g} represents the electronic bandgap.[40] The exciton binding energy represents the coulombic interaction between electrons and holes and is typically observed as a smaller bandgap. The difference between the optical and electronic bandgap corresponds to the excitonic states located below the bandgap minimum, indicating that Bi doping introduces shallow trap states below the CBM. It is worth noting that Bi-doped

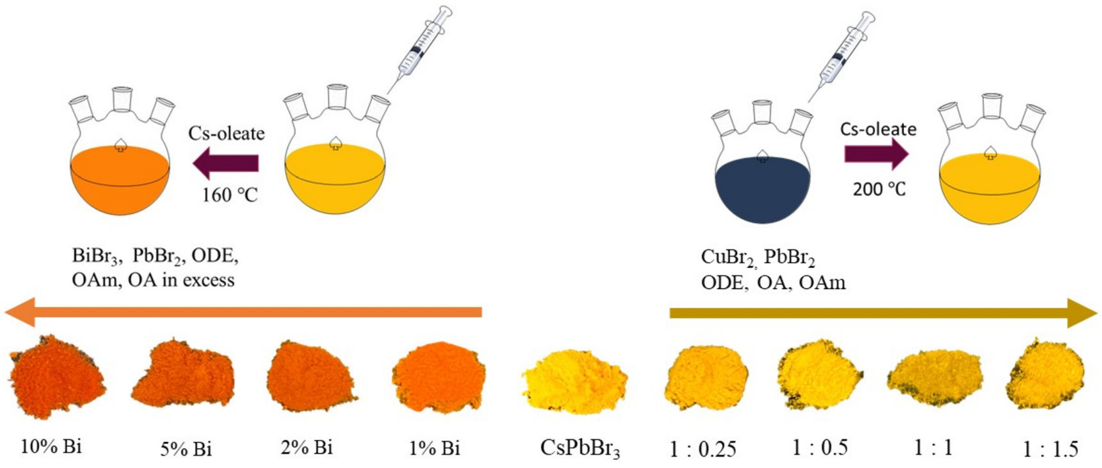

Fig. 1 Photographs of Bi- and Cu-doped $CsPbBr_3$ powders obtained after synthesis.

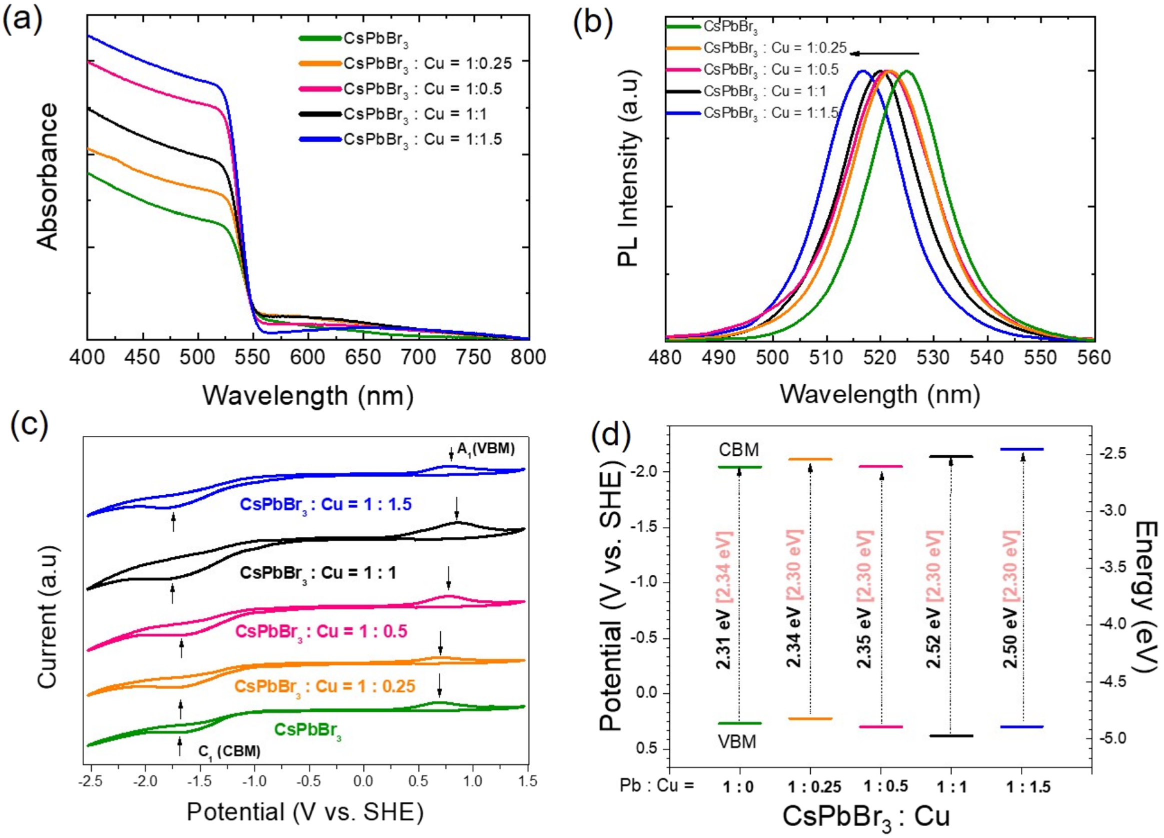

Fig. 2 (a) UV-visible absorption spectra and (b) emission spectra of Cu-doped $CsPbBr_3$ nanoparticles. (c) Cyclic voltammograms of Cu-doped $CsPbBr_3$ recorded at 50 mV s^{-1} in a 100 mM solution of $(Bu_4N)(PF_6)$ in DCM, showing oxidation (A_1) and reduction (C_1) peaks. (d) Energy band edge diagrams of Cu-$CsPbBr_3$ MHPs deduced from (c). Electrochemical bandgap values (E_g^{qp}, black) were compared with optical ones (E_g^{opt}, pale pink).

$CsPbBr_3$ demonstrated an upward shift of the conduction bandgap minimum (CBM), while the valence band maximum (VBM) remains at an energy level similar to that of pristine $CsPbBr_3$ synthesized at 160 °C. Furthermore, the average bandgap energy estimated from the CV measurements is 0.3 eV higher than that of pristine $CsPbBr_3$, consistent with previous studies.[26]

X-ray diffraction (XRD) patterns of each $CsPbBr_3$ powder obtained using different doping amounts of Cu showed no extra peaks (Fig. 4a) compared with the undoped $CsPbBr_3$ nanocrystal (Fig. S4), indicating an orthorhombic single-phase material that retains the structural framework of pure $CsPbBr_3$ crystals, which were further confirmed using transmission electron microscopy (TEM) and fast Fourier transform (FFT) analysis (Fig. S5 and S6). The morphology of Cu-doped $CsPbBr_3$ was observed by TEM, and the results are shown in Fig. 4b and Fig. S7a–c. TEM images revealed cubic morphologies of Cu-doped $CsPbBr_3$ nanoparticles, with average sizes of 37, 20, and 21 nm when the ratio between Pb : Cu was 1 : 0.25, 1 : 0.5 and 1 : 1.5, respectively (Fig. S7). The $CuBr_2$ treatment of $CsPbBr_3$ at 200 °C did not affect the shape and size of Cu-$CsPbBr_3$, except at the 1 : 0.25 doping level, where the particle size was twice that of pristine MHPs (~20 nm). For the Pb : Cu = 1 : 1 sample, we could also assign orthorhombic $CsPbBr_3$ (ICSD: 97851) NPs (Fig. S8a–e). The nanoparticles were oriented along the [101] or [210] zone axes (Fig. S8d and e). Similarly, at a higher doping ratio (1 : 1.5), the FFT analysis of the image revealed that the NPs adopted an orthorhombic $CsPbBr_3$ structure. Despite Cu doping, we did not observe significant changes in the *d*-spacings and angles with respect to the reported $CsPbBr_3$ crystal structure (Fig. 4b and Fig. S9), which is consistent with the XRD analysis, showing no evidence of any significant change in the lattice parameters of the orthorhombic structure. The Cu-doped $CsPbBr_3$ nanoparticles maintained the same zone axis orientation. Moreover, energy-dispersive X-ray spectroscopy (EDS) mapping demonstrated a homogeneous distribution of Cs, Pb, and Br atoms (Fig. 4d). Electron energy loss spectroscopy (EELS), combined with principal component analysis (PCA), was applied to the image shown in Fig. 4c, to analyze elemental signal within the sample. Close-up spectra of individual elemental edges are shown in Fig. S10. Note that no Cu signal from the $L_{3,2}$ edges was detected, which should appear at 931 and 951 eV. We can hypothesize that the intense signal from Cs might be suppressing the detection of the Cu signal.

X-ray diffraction (XRD) patterns indicate that the perovskite retains its orthorhombic structure upon treatment with a variable ratio of $BiBr_3$ (Fig. 5a). The synthesis of Bi-doped MHP

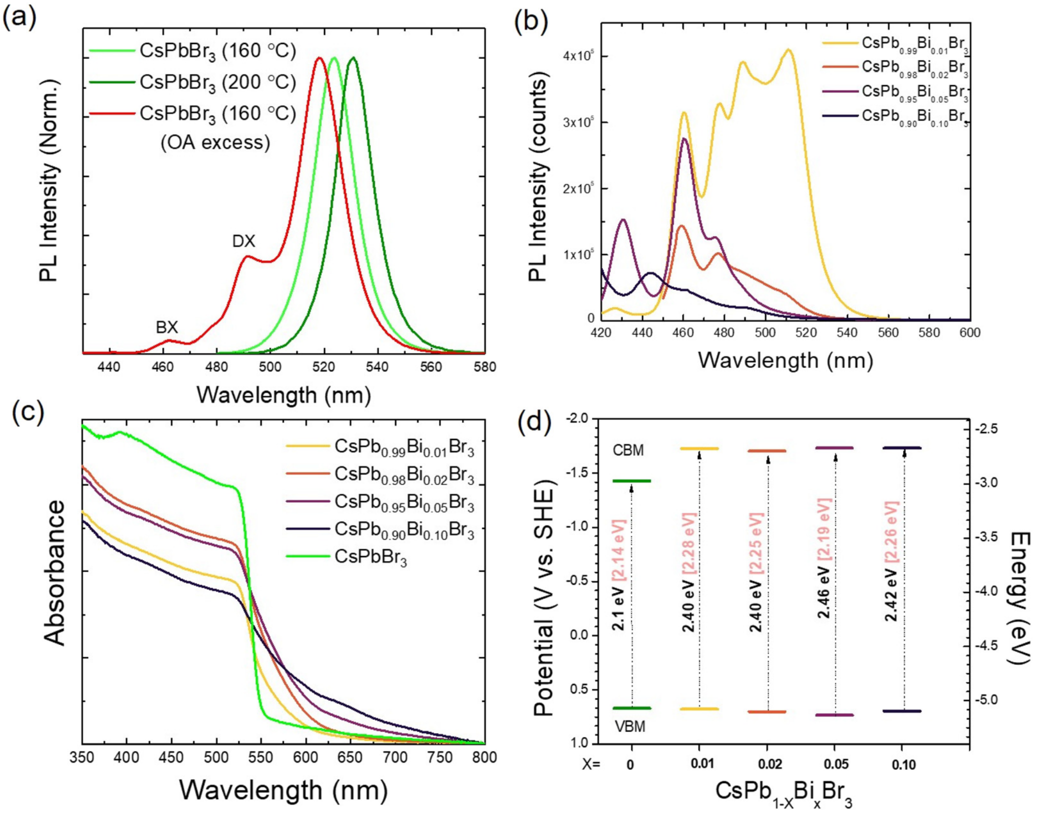

Fig. 3 (a) Emission spectra of $CsPbBr_3$ synthesized at 160 °C, 200 °C, and 160 °C with modified OA : OAm ratio. (b) Photoluminescence spectra of variable samples of Bi-doped $CsPbBr_3$. (c) Absorption spectra of variable Bi-doping $CsPbBr_3$ obtained at 160 °C. (d) Electrochemical bandgap values (E_g^{qp}, black) were compared with optical ones (E_g^{opt}, pale pink).

was performed at 160 °C. Thus, for comparison, TEM images of undoped $CsPbBr_3$ are shown in Fig. S11. The images show well-dispersed nanocrystals with an average size of 16 nm. The morphology of $CsPbBr_3$ shows the formation of $CsPbBr_3$ nanosheets with a limited number of nanocubes.[41] In contrast, we observe that the nanosheets are thinner than the nanocubes, with variable aspect ratios. Higher TEM magnification of Bi-doped $CsPbBr_3$ indicates that the hot-injection synthesis at 160 °C yields nanocubes of variable sizes, *ca.* 10, 20, and 40 nm, with no formation of Bi nanoparticles. The shape of the MHP appears to change as the doping ratio increases, leading to the formation of 2D perovskite with variable aspect ratios (Fig. 5b, c and Fig. S12a–h). These 2D perovskites are mainly observed at lower doping ratios (less than 10%). The broad size distribution and the formation of the 2D perovskite rationalize the multiple-emission spectra observed in Fig. 3b. The 2D perovskite comprises varying aspect ratios and retains some 3D perovskite, leading to variable exciton relaxation behavior and translating variable photoluminescence peaks. A reduced dimension or thinner layer results in blue-shifted photoluminescence and a lower bandgap value. The FFT analysis of the image reveals that the NPs adopt an orthorhombic $CsPbBr_3$ structure (ICSD: 97851), consistent with the XRD patterns (Fig. 5e). Nanoparticles were oriented along the [101] zone axis.

X-ray photoelectron spectroscopy (XPS) surface analysis was performed to demonstrate the presence of Bi and Cu in the doped perovskite. The survey and the high-resolution spectra of the samples indicate the presence of Cs, Pb, and Br in all doped and undoped $CsPbBr_3$ (Fig. S13 and S14). High-resolution XPS spectra show the presence of oxygen in $CsPbBr_3$, which could originate from OA binding to the surface, with a signal located at 532.1 eV (Fig. S14). The Cs 3d spectra of doped $CsPbBr_3$ originate from $3d_{3/2}$ and $3d_{5/2}$ spin–orbit coupling, located at 724.5 and 738.4 eV, respectively (Fig. 6a). The Pb 4f peaks are split into $4f_{7/2}$ and $4f_{5/2}$, located at 138.2 and 143.1 eV, respectively (Fig. 6a). The high-resolution Br 3d spectra are centered at 68.1 and 68.3 eV (Fig. 6a). All peaks are similar to those obtained for Cu-doped perovskites and do not exhibit any significant shift compared to pristine $CsPbBr_3$ (Fig. S14). XPS analysis confirms the presence of Bi^{3+} as the doping is performed. The Bi $4f_{5/2}$ component is distinguishable at a binding energy 164.3 eV, as shown in Fig. 6b. The Bi 4f region splits into two components, including Bi $4f_{7/2}$, which obviously overlaps with the Cs $4P_{3/2}$ component at 158.9 eV.[11,42] The Cu-doped perovskites exhibit Cu 2p transitions, with two main contributions located at around 931.3 and 936.0 eV, as shown in Fig. 6c. These contributions are likely to translate into contributions that can be attributed to Cu^{2+} species in different coordination.[43,44] The first peak is shifted

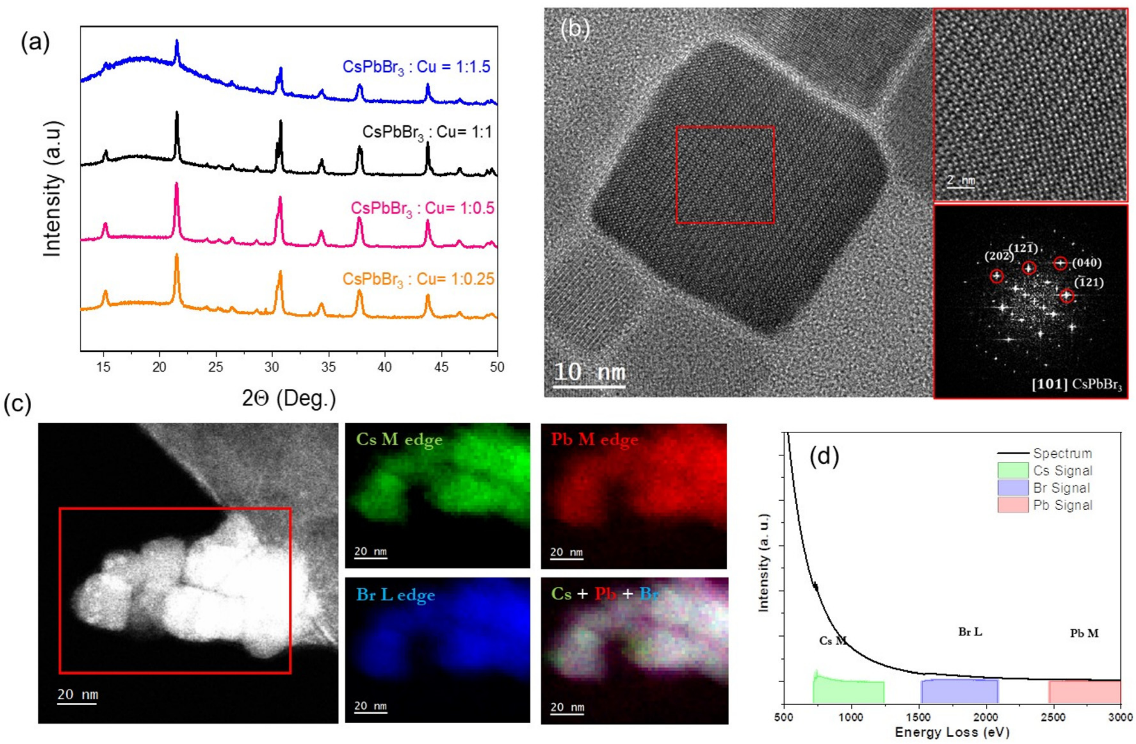

Fig. 4 (a) Powder XRD patterns of Cu-doped CsPbBr$_3$ nanocrystals prepared from solutions containing variable amounts of the dopant precursor. (b) HR-TEM images of CsPbBr$_3$: Cu = 1 : 1.5 and its FFT analysis. (c) EDS elemental mappings of CsPbBr$_3$: Cu = 1 : 1.5. (d) EELS analysis of the selected region from (c). Note that the crystal lattices in the micrograph of the region of interest have been enhanced using a frequency filter in the reciprocal space.

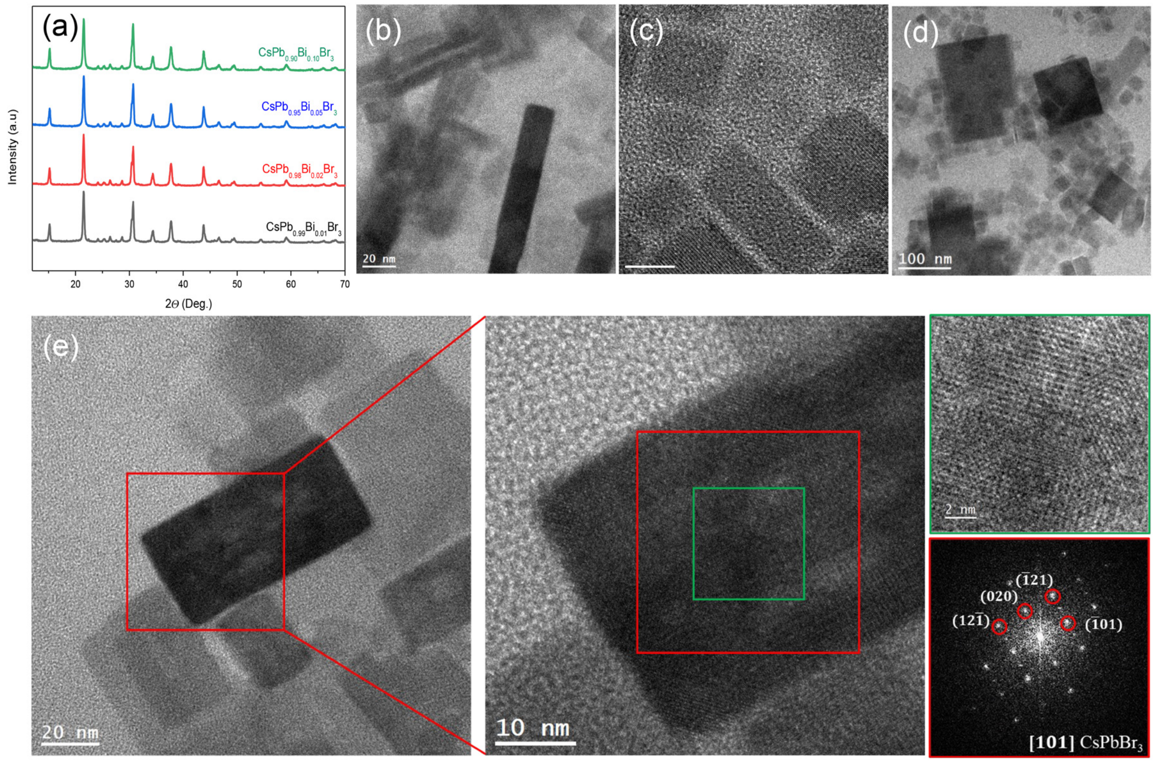

Fig. 5 (a) Powder XRD patterns of Bi-doped CsPbBr$_3$ nanocrystals prepared using solutions containing variable amounts of the dopant precursor. TEM images of CsPbBr$_3$ doped with (b) 1%, (c) 5%, and (d) 10% of Bi obtained at 160 °C. (e) HR-TEM images of CsPbBr$_3$ doped with 10% Bi and its FFT analysis. The crystal lattices in the micrograph of the region of interest have been enhanced using a frequency filter in the reciprocal space.

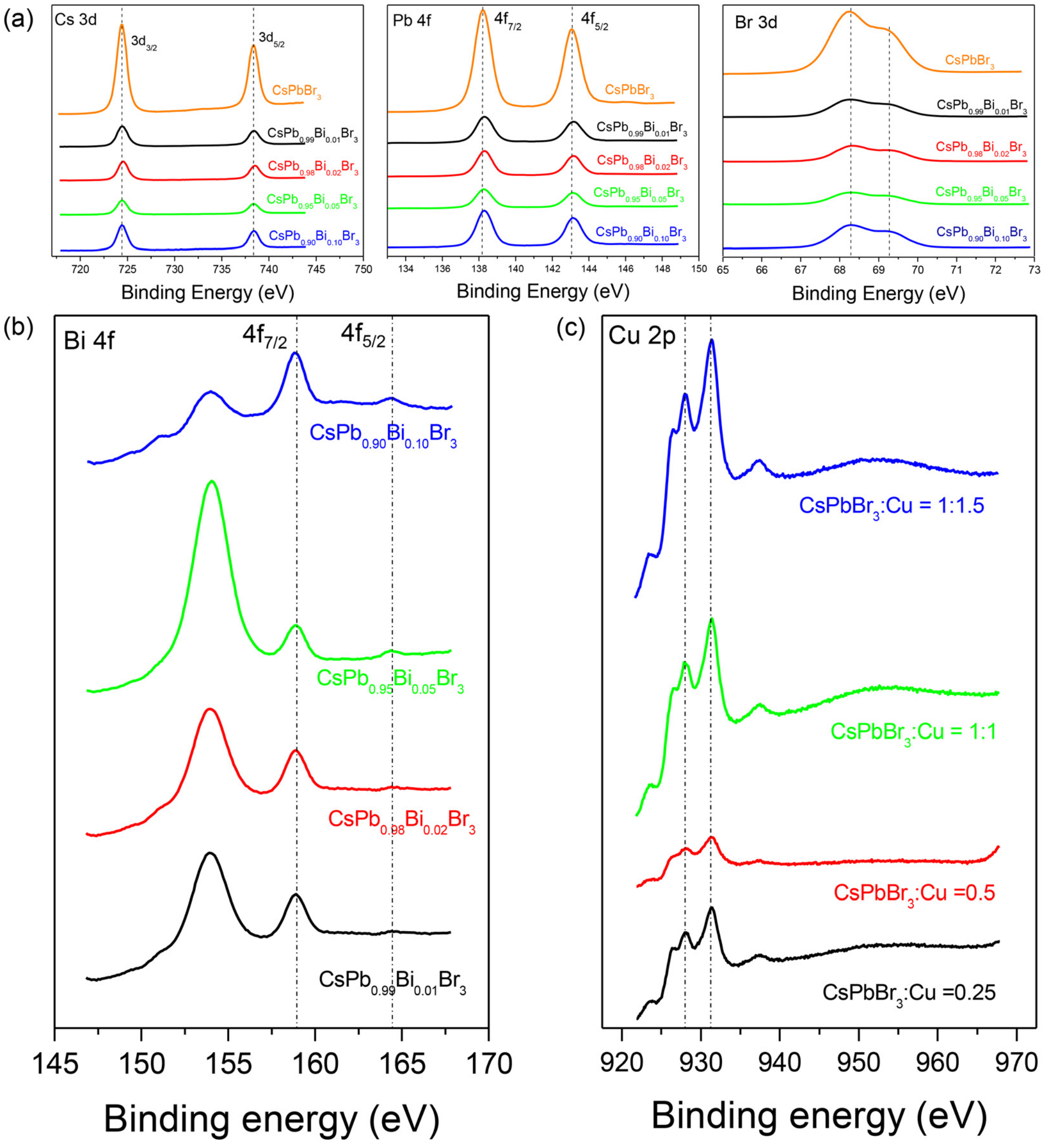

Fig. 6 High-resolution XPS spectra of (a) Cs, Pb, and Br in Bi-doped $CsPbBr_3$, (b) Bi in Bi-doped $CsPbBr_3$, and (c) Cu in Cu-doped $CsPbBr_3$.

to lower energy compared to that reported for tetracoordinated Cu. However, the peak centered at *ca.* 937 eV corresponds to isolated Cu^{2+} in octahedral coordination, consistent with the substitution of the Pb atom into the perovskite structure. The Cu 2p region overlaps with a peak at 928.1 eV, assigned to Cs MMNT.

The photocatalytic activities of Bi- and Cu-doped $CsPbBr_3$ NCs were evaluated for toluene oxidation under xenon lamp illumination for 3 h (Fig. 7). The photocatalytic activity showed a significant improvement in the oxidation of toluene due to Bi doping (Fig. 7a). We observed enhanced photocatalytic activity with Bi doping of $CsPbBr_3$, irrespective of the ratio. The photocatalytic efficiency exhibited a maximum oxidation rate at 1% and 10% doping levels. The linear conversion trend of toluene to benzaldehyde during 3 h of illumination indicates the stability of the photocatalyst throughout the reaction. The photocatalytic oxidation rate increased from 171 ppm g^{-1} min^{-1} for undoped $CsPbBr_3$ to 435 and 411 ppm g^{-1} min^{-1} for $CsPb_{0.99}Bi_{0.01}Br_3$ and $CsPb_{0.90}Bi_{0.10}Br_3$, respectively (Fig. 7b). We also assessed the photocatalytic properties of Cu-doped $CsPbBr_3$ NCs. The photocatalytic toluene oxidation improved significantly compared to undoped $CsPbBr_3$. The photocatalytic activity increased gradually, reaching an optimum at a Pb/Cu ratio of 1 : 1, with a conversion of 80 × 10^3 ppm g^{-1} after 3 h of reaction. However, excessive doping (1 : 1.5) led to a drop in the benzaldehyde production, which was inferior to that of the undoped $CsPbBr_3$ NCs. The rate of toluene photocatalytic oxidation reached 460 ppm g^{-1} min^{-1},[1] closely comparable to that of Bi-doped $CsPbBr_3$ (Fig. 7b).

The photocatalytic oxidation of toluene under UV-Vis illumination produces benzaldehyde as the main product, with benzylic alcohol as an intermediate. The key to successful

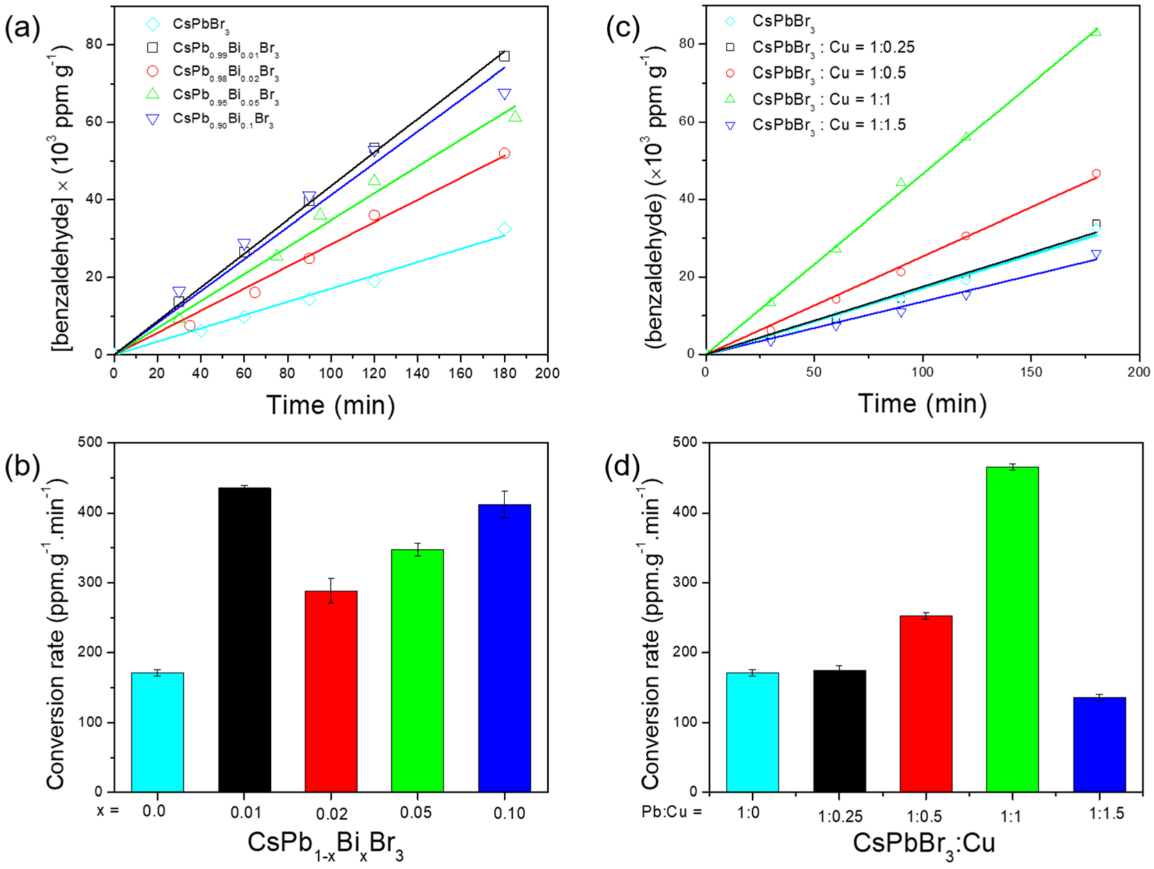

Fig. 7 Photocatalytic activity and toluene conversion rate under UV-Vis illumination for 3 hours over Bi-doped $CsPbBr_3$ (a and b) and Cu-doped $CsPbBr_3$ (c and d) photocatalysts.

toluene oxidation is pre-saturation with oxygen, which allows the generation of superoxide anion radicals ($O_2^{\bullet-}$) in the presence of electrons (eqn (2)). The rate-determining step in toluene oxidation involves C(sp^3)–H bond activation of adsorbed toluene on the photocatalyst surface, upon interaction with holes on the MHPs site (eqn (3)).[19,45–48]

$$O_2 + e^- \rightarrow O_2^{\bullet-} \qquad (2)$$

$$C_6H_5CH_3 + h^+ \rightarrow C_6H_5CH_2^{\bullet} \qquad (3)$$

The proposed mechanism of toluene oxidation is given by the following equations:

$$C_6H_5CH_2^{\bullet} + O_2 \rightarrow C_6H_5CH_2OO^{\bullet} \qquad (4)$$

$$C_6H_5CH_2OO^{\bullet} + C_6H_5CH_2^{\bullet} \rightarrow C_6H_5CH_2OH + C_6H_5CHO \qquad (5)$$

$$C_6H_5CH_2^{\bullet} + O_2^{\bullet-} \rightarrow C_6H_5CH_2OO^- \qquad (6)$$

$$C_6H_5CH_2OO^- + H^+ \rightarrow C_6H_5CH_2OOH \xrightarrow{-H_2O} C_6H_5CHO. \qquad (7)$$

Photogenerated charge carriers play a major role in toluene oxidation. To investigate the effects of bismuth and copper on these carriers, time-resolved photoluminescence spectroscopy was performed. When $CsPbBr_3$ was doped with bismuth, its photoluminescence was dramatically quenched. The average PL lifetime decreased from 17.5 ns in undoped $CsPbBr_3$ (160 °C) to 1.3 ns (Fig. 8a and Table S1). On the other hand, undoped $CsPbBr_3$ nanosheets prepared under the same conditions exhibited an even longer lifetime of 28.9 ns. Bismuth introduces shallow states just below the conduction band minimum, acting as electron-type trapping states.[11] These additional states can trap electrons, leading to PL quenching. Copper doping gradually reduced the photoluminescence lifetime, but an excessive Cu content (Pb : Cu = 1 : 1.5) led to an increase in lifetime, contrary to earlier reports that show enhancement at low doping and suppression at higher levels (Fig. 8b and Table S2).[7] The PL lifetime decay profile was fitted using a multiexponential fit, and the average lifetime decreased to 1.4 ns at a Pb : Cu ratio of 1 : 1. Interestingly, at Pb : Cu = 1 : 1.5, the lifetime increased to 6.2 ns, although this value remains much lower than that observed for undoped $CsPbBr_3$.

In summary, low bismuth doping generates shallow traps that capture electrons and facilitate the formation of oxygen radicals, thereby participating in charge carrier separation, which is reflected in the reduction of photoluminescence (PL) lifetime. Consequently, holes remain free for the activation of C(sp^3)–H bonds, resulting in the generation of benzylic radicals. However, further doping with bismuth does not yield a

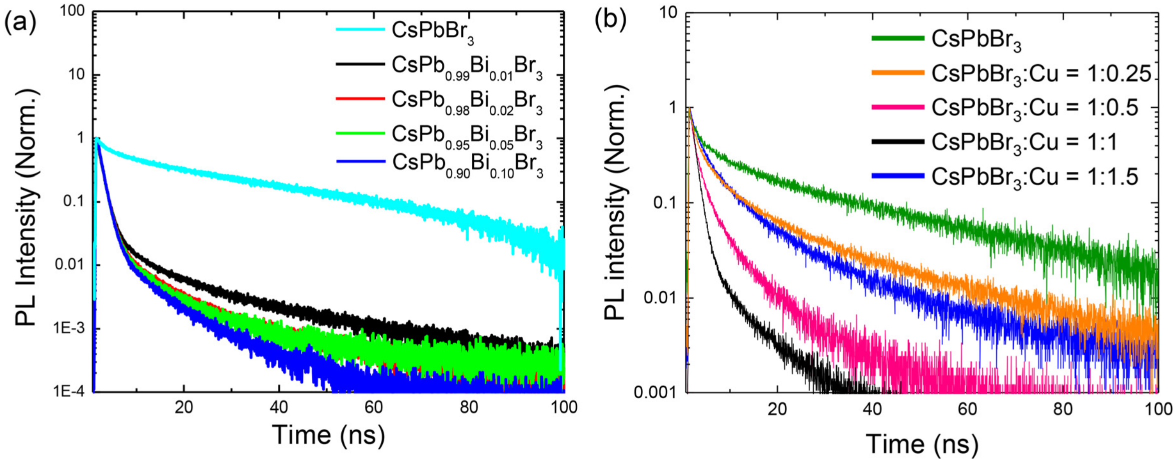

Fig. 8 TRPL lifetime decay of (a) Bi-doped CsPbBr$_3$ and (b) Cu-doped CsPbBr$_3$ upon laser excitation at 375 nm.

beneficial effect on the photocatalytic oxidation of toluene, except at a higher bismuth doping ratio. At elevated doping levels, the effects are expected to be more pronounced due to the reduced PL lifetime, which leads to enhanced photocatalytic activity. Additionally, copper appears to act as an electron collector, although to a limited extent. Indeed, the quenching of PL is interpreted as a result of copper creating shallow traps that capture electrons, thus leaving free holes for the oxidation reaction. Nevertheless, an excessive loading of copper leads to photocatalytic deactivation, which may originate from the formation of deep traps within the band structure that function as recombination sites.

Conclusion

Herein, we achieved Bi and Cu doping of CsPbBr$_3$ using the hot-injection method. We found that the effect of doping on the optical, electronic, morphological, and photocatalytic activity depends on the nature of the cation used. For Bi doping of CsPbBr$_3$, only a small amount of BiBr$_3$ is necessary to initiate the reaction. It is crucial to maintain the synthetic reaction temperature at 160 °C to avoid the Bi reduction and formation of metallic nanoparticles. A reduction in the temperature led to the formation of 2D perovskite nanosheets with varying aspect ratios. However, doping with copper requires a significantly higher amount of CuBr$_2$ to initiate doping owing to the higher energy required to form the Cu–Br bond compared to the Pb–Br bond. We found that the bandgap energy increased with Bi and Cu doping, indicating the introduction of a trap state. The band-tail in the absorption spectrum of Bi-doped MHP suggests the generation of shallow trap states in the conduction band. Both metals indicate photoluminescence quenching, demonstrating charge transfer from MHP to either the Bi or Cu trap states. We found that the photocatalytic activity toward toluene oxidation improved upon doping. However, the mechanism behind this enhancement varies depending on the cation used. Copper doping exhibited remarkable photocatalytic activity and stability during 3 h reactions. The optimal photocatalytic activity was achieved at a nominal Cu ratio of 0.5 (Pb : Cu = 1 : 0.5), surpassing that of Bi-doped MHP. Unlike bismuth, which incorporates trap states below the conduction band minimum (CBM), copper influences both the conduction and valence band positions, making the oxidation reaction more favorable.

Author contributions

M. Knezevich and T.-H. Hoang carried out the experiments and investigation process, curated the data, wrote the initial draft, and reviewed and edited the final manuscript. V. D. Quach performed the PEC experiments. A. G. Manjón, D. Llorens Rauret, and J. Arbiol performed the electron microscopy analyses and discussed their results. M. Erard and A. Gayral performed the TRPL measurements and discussed the results. D. Berardan performed the XRD analysis and discussed the result. M. Benoit supervised the HPLC analysis and set up the analytical method. C. Colbeau-Justin supervised the study. M. N. Ghazzal conceptualized and conceived the idea, acquired the financing, supervised the work, contributed to the manuscript structure, and reviewed and edited the final manuscript. The manuscript was written with the help of all the co-authors.

Conflicts of interest

The authors declare that no conflict of interest, financial or otherwise, exists.

Data availability

The data that support the findings of this study are available from the corresponding author upon reasonable request.

Supplementary information such as TEM, Kubelka-Munk calculations, XRD, Cyclic voltammograms, EELS spectra, XPS and TRPL is available. See DOI: **https://doi.org/10.1039/d5nr02442k**.

Acknowledgements

MK acknowledges the French "Ministère de l'enseignement supérieur et de la recherche" (MESR) for the PhD Grant. MNG thanks the public grant overseen by the French National Research Agency (ANR) through the IngenCat project (ANR-20-CE43-0014) and the NEXTCCUS project as part of the ERANET-ACT3 call program for the financial support. The authors thank François Brisset for his valuable help in performing the TEM analysis. The authors thank Diana Dragoe for her valuable help in performing the XPS analysis. ICN2 is supported by the Severo Ochoa program from the Spanish MCIN/AEI (grant no.: CEX2021-001214-S) and is funded by the CERCA Programme from the Generalitat de Catalunya. ICN2 acknowledges funding from the Generalitat de Catalunya 2021SGR00457. The authors thank for the support from the project AMaDE (PID2023-149158OB-C43), funded by MCIN/AEI/10.13039/501100011033/ and by "ERDF A way of making Europe", by the "European Union". AGM acknowledges the RyC Programme by MCIN/AEI and Ayuda RYC2021-033479-I funded by MCIN/AEI/10.13039/501100011033 and by the European Union NextGenerationEU/PRTR. Part of the present work was performed in the framework of Universitat Autònoma de Barcelona Materials Science PhD program. ICN2 is a founding member of e-DREAM.[49]

References

1 I. Chung, B. Lee, J. He, R. P. H. Chang and M. G. Kanatzidis, *Nature*, 2012, **485**, 486–489.
2 F. Hao, C. C. Stoumpos, D. H. Cao, R. P. H. Chang and M. G. Kanatzidis, *Nat. Photonics*, 2014, **8**, 489–494.
3 M. Knezevic, T.-H. Hoang, N. Rashid, M. Abdi-Jalebi, C. Colbeau-Justin and M. N. Ghazzal, *Sci. China Mater.*, 2023, **66**, 2545–2572.
4 V. K. Ravi, G. B. Markad and A. Nag, *ACS Energy Lett.*, 2016, **1**, 665–671.
5 M. V. Kovalenko, L. Protesescu and M. I. Bodnarchuk, *Science*, 2017, **358**, 745–750.
6 M. Knezevic, V.-D. Quach, I. Lampre, M. Erard, P. Pernot, D. Berardan, C. Colbeau-Justin and M. N. Ghazzal, *J. Mater. Chem. A*, 2023, **11**, 6226–6236.
7 C. Bi, S. Wang, Q. Li, S. V. Kershaw, J. Tian and A. L. Rogach, *J. Phys. Chem. Lett.*, 2019, **10**, 943–952.
8 N. Mondal, A. De and A. Samanta, *ACS Energy Lett.*, 2019, **4**, 32–39.
9 W. Van Der Stam, J. J. Geuchies, T. Altantzis, K. H. W. Van Den Bos, J. D. Meeldijk, S. Van Aert, S. Bals, D. Vanmaekelbergh and C. De Mello Donega, *J. Am. Chem. Soc.*, 2017, **139**, 4087–4097.
10 A. Shapiro, M. W. Heindl, F. Horani, M.-H. Dahan, J. Tang, Y. Amouyal and E. Lifshitz, *J. Phys. Chem. C*, 2019, **123**, 24979–24987.
11 R. Begum, M. R. Parida, A. L. Abdelhady, B. Murali, N. M. Alyami, G. H. Ahmed, M. N. Hedhili, O. M. Bakr and O. F. Mohammed, *J. Am. Chem. Soc.*, 2017, **139**, 731–737.
12 B. Yang and K. Han, *Acc. Chem. Res.*, 2019, **52**, 3188–3198.
13 E. M. Hutter, M. C. Gélvez-Rueda, D. Bartesaghi, F. C. Grozema and T. J. Savenije, *ACS Omega*, 2018, **3**, 11655–11662.
14 D. Bartesaghi, A. H. Slavney, M. C. Gélvez-Rueda, B. A. Connor, F. C. Grozema, H. I. Karunadasa and T. J. Savenije, *J. Phys. Chem. C*, 2018, **122**, 4809–4816.
15 Y.-W. Liu, S.-H. Guo, S.-Q. You, C.-Y. Sun, X.-L. Wang, L. Zhao and Z.-M. Su, *Nanotechnology*, 2020, **31**, 215605.
16 J. Yin, G. H. Ahmed, O. M. Bakr, J.-L. Brédas and O. F. Mohammed, *ACS Energy Lett.*, 2019, **4**, 789–795.
17 M. Liu, G. Zhong, Y. Yin, J. Miao, K. Li, C. Wang, X. Xu, C. Shen and H. Meng, *Adv. Sci.*, 2017, **4**, 1700335.
18 B.-M. Bresolin, C. Günnemann, D. W. Bahnemann and M. Sillanpää, *Nanomaterials*, 2020, **10**, 763.
19 Y. Dai, C. Poidevin, C. Ochoa-Hernández, A. A. Auer and H. Tüysüz, *Angew. Chem.*, 2020, **132**, 5837–5845.
20 M. Miodyńska, A. Mikolajczyk, P. Mazierski, T. Klimczuk, W. Lisowski, G. Trykowski and A. Zaleska-Medynska, *Appl. Surf. Sci.*, 2022, **588**, 152921.
21 Y. Ji, M. She, X. Bai, E. Liu, W. Xue, Z. Zhang, K. Wan, P. Liu, S. Zhang and J. Li, *Adv. Funct. Mater.*, 2022, **32**, 2201721.
22 L. Romani, A. Speltini, C. N. Dibenedetto, A. Listorti, F. Ambrosio, E. Mosconi, A. Simbula, M. Saba, A. Profumo, P. Quadrelli, F. De Angelis and L. Malavasi, *Adv. Funct. Mater.*, 2021, **31**, 2104428.
23 C. Barman, S. Lavadiya, S. K. Nayak, V. R. Soma and S. S. K. Raavi, *ACS Appl. Nano Mater.*, 2025, **8**, 2238–2248.
24 F. N. Mansoorie, P. Bhatt, A. Tewari, R. Kumar and M. Bag, *ACS Appl. Mater. Interfaces*, 2025, **17**, 4218–4230.
25 Z. Ma, P. Lv, X. He, F. Wang, Y. Li, G. Xiao and B. Zou, *Nano Lett.*, 2025, **25**, 9345–9352.
26 O. A. Lozhkina, A. A. Murashkina, V. V. Shilovskikh, Y. V. Kapitonov, V. K. Ryabchuk, A. V. Emeline and T. Miyasaka, *J. Phys. Chem. Lett.*, 2018, **9**, 5408–5411.
27 L. Li and Z. Zhang, *Chem. Eng. J.*, 2022, **434**, 134811.
28 L. Protesescu, S. Yakunin, M. I. Bodnarchuk, F. Krieg, R. Caputo, C. H. Hendon, R. X. Yang, A. Walsh and M. V. Kovalenko, *Nano Lett.*, 2015, **15**, 3692–3696.
29 C. Lu, M. W. Wright, X. Ma, H. Li, D. S. Itanze, J. A. Carter, C. A. Hewitt, G. L. Donati, D. L. Carroll, P. M. Lundin and S. M. Geyer, *Chem. Mater.*, 2019, **31**, 62–67.
30 F. Ye, H. Zhang, W. Li, Y. Yan, J. Cai, R. S. Gurney, A. J. Pearson, D. Liu and T. Wang, *Small Methods*, 2019, **3**, 1800489.
31 F. Ye, H. Zhang, W. Li, Y. Yan, J. Cai, R. S. Gurney, A. J. Pearson, D. Liu and T. Wang, Ligand–Exchange of

Low–Temperature Synthesized $CsPbBr_3$ Perovskite toward High–Efficiency Light–Emitting Diodes, *Small Methods*, 2019, **3**, 1800489.

32 D. Lee, M. Kim, H.-Y. Woo, J. Chae, D. Lee, S. Jeon, S. J. Oh and T. Paik, *RSC Adv.*, 2020, **10**, 7126–7133.

33 Z. Wang, C. Jiang, R. Huang, H. Peng and X. Tang, *J. Phys. Chem. C*, 2014, **118**, 1155–1160.

34 D. Velasco-Arias, I. Zumeta-Dubé, D. Díaz, P. Santiago-Jacinto, V.-F. Ruiz-Ruiz, S.-E. Castillo-Blum and L. Rendón, *J. Phys. Chem. C*, 2012, **116**, 14717–14727.

35 B. Wang, L. Liu, B. Liu, J. Li, B. Cao, Z. Zhao and Z. Liu, *Phys. B*, 2020, **599**, 412488.

36 M. Laitz, A. E. K. Kaplan, J. Deschamps, U. Barotov, A. H. Proppe, I. García-Benito, A. Osherov, G. Grancini, D. W. deQuilettes, K. A. Nelson, M. G. Bawendi and V. Bulović, *Nat. Commun.*, 2023, **14**, 2426.

37 T. T. H. Do, A. Granados del Águila, D. Zhang, J. Xing, S. Liu, M. A. Prosnikov, W. Gao, K. Chang, P. C. M. Christianen and Q. Xiong, *Nano Lett.*, 2020, **20**, 5141–5148.

38 A. C. Jakowetz, M. L. Böhm, A. Sadhanala, S. Huettner, A. Rao and R. H. Friend, *Nat. Mater.*, 2017, **16**, 551–557.

39 G. Rey, G. Larramona, S. Bourdais, C. Choné, B. Delatouche, A. Jacob, G. Dennler and S. Siebentritt, *Sol. Energy Mater. Sol. Cells*, 2018, **179**, 142–151.

40 S. N. Inamdar, P. P. Ingole and S. K. Haram, *ChemPhysChem*, 2008, **9**, 2574–2579.

41 Q. Zhang, F. Diao, X. Xue, X. Sheng, D. Barba and Y. Wang, *ACS Appl. Mater. Interfaces*, 2021, **13**, 44777–44785.

42 K. Marjit, G. Ghosh, R. K. Biswas, S. Ghosh, S. K. Pati and A. Patra, *J. Phys. Chem. Lett.*, 2022, **13**, 5431–5440.

43 B. Pereda-Ayo, U. De La Torre, M. J. Illán-Gómez, A. Bueno-López and J. R. González-Velasco, *Appl. Catal., B*, 2014, **147**, 420–428.

44 V.-D. Quach, M. C. Spadaro, D. Dragoe, M. Botifoll, H. Vezin, C. Colbeau-Justin, F. Dumeignil, J. Arbiol, R. Wojcieszak and M. N. Ghazzal, *J. Mater. Chem. A*, 2024, **12**, 19236–19246.

45 Y. Dai and H. Tüysüz, *Sol. RRL*, 2021, **5**, 2100265.

46 L.-Y. Pan, Y.-F. Ding, S.-F. Yin and M.-Q. Cai, *New J. Chem.*, 2022, **46**, 16922–16931.

47 J. Li, X. Wang, H. Fang, X. Guo, R. Zhou, C. Wang, J. Li, M. N. Ghazzal and Z. Rui, *J. Mater. Chem. A*, 2023, **11**, 25639–25649.

48 J. Li, H. Fang, M. Wu, C. Ma, R. Lian, S. P. Jiang, M. N. Ghazzal and Z. Rui, *Small*, 2023, **19**, 2300559.

49 R. Ciancio, R. E. Dunin-Borkowski, E. Snoeck, M. Kociak, R. Holmestad, J. Verbeeck, A. I. Kirkland, G. Kothleitner and J. Arbiol, *Microsc. Microanal.*, 2022, **28**, 2900–2902.